CM^2 Magazine

第 140 期

南方科技大学海洋磁学中心主编

https://cm2.sustech.edu.cn/

创刊词

海洋是生命的摇篮，是文明的纽带。地球上最早的生命诞生于海洋，海洋里的生命最终进化成了人类，人类的文化融合又通过海洋得以实现。人因海而兴。

人类对海洋的探索从未停止。从远古时代美丽的神话传说，到麦哲伦的全球航行，再到现代对大洋的科学钻探计划，海洋逐渐从人类敬畏崇拜幻想的精神寄托演变成可以开发利用与科学研究的客观存在。其中，上个世纪与太空探索同步发展的大洋科学钻探计划将人类对海洋的认知推向了崭新的纬度：深海（deep sea）与深时（deep time）。大洋钻探计划让人类知道，奔流不息的大海之下，埋藏的却是亿万年的地球历史。它们记录了地球板块的运动，从而使板块构造学说得到证实；它们记录了地球环境的演变，从而让古海洋学方兴未艾。

在探索海洋的悠久历史中，从大航海时代的导航，到大洋钻探计划中不可或缺的磁性地层学，磁学发挥了不可替代的作用。这不是偶然，因为从微观到宏观，磁性是最基本的物理属性之一，可以说，万物皆有磁性。基于课题组的学科背景和对海洋的理解，我们对海洋的探索以磁学为主要手段，海洋磁学中心因此而生。

海洋磁学中心，简称 CM^2，一为其全名“Centre for Marine Magnetism”的缩写，另者恰与爱因斯坦著名的质能方程 $E = MC^2$ 对称，借以表达我们对科学巨匠的敬仰和对科学的不懈追求。

然而科学从来不是单打独斗的产物。我们以磁学为研究海洋的主攻利器，但绝不仅限于磁学。凡与磁学相关的领域均是我们关注的重点。为了跟踪反映国内外地球科学特别是与磁学有关的地球科学领域的最新研究进展，海洋磁学中心特地主办 CM^2 Magazine，以期与各位地球科学工作者相互交流学习、合作共进！

“海洋孕育了生命，联通了世界，促进了发展”。21 世纪是海洋科学的时代，由陆向海，让我们携手迈进中国海洋科学的黄金时代。

目 录

1. 陆地证据显示海因里希事件发生时海洋过程与劳伦冰盖的冰下水文相互作用

翻译人：仲义 zhongy@sustech.edu.cn

Edwards, G. H., Blackburn, T., Piccione, G., et al. ***Terrestrial evidence for ocean forcing of Heinrich events and subglacial hydrologic connectivity of the Laurentide Ice Sheet*** *[J] Science Advance, 2022, 8(42), eabp9329.*

https://doi.org/10.1126/sciadv.abp9329

摘要：在末次冰期期间，劳伦冰盖（Laurentide Ice Sheet）经历了多次快速的冰盖融化时间，并在海洋沉积物所记录下来，被称为“海因里希事件”（Heinrich events）。两种相互竞争的模型试图通过内部冰盖震荡过程或者海洋气候强迫来描述对于海因里希事件的成因。本文作者通过来自劳伦冰盖东北部海因里希事件发生时的陆上记录有力地支持了海洋气候强迫作用的重要性。通过来自巴芬岛的冰下碳酸盐沉积记录了冰下融化的事件，与最近三次海因里希事件发生时间相一致，这是由于附近海洋环流末端冰流的加速所造成的。巴芬岛和哈德逊海峡的同步冰流加速与内部冰盖震荡本身不一致，表明有共同的海洋气候因子协调这些不同的冰川系统。这些沉积记录下来的同位素组成记录了冰盖下广泛分布地下水的连通性。在海因里希末期广泛出现含水层的基底融化和冲刷作用可能是末次冰川消退的前兆。

ABSTRACT: During the last glacial period, the Laurentide Ice Sheet (LIS) underwent episodes of rapid iceberg discharge, recorded in ocean sediments as “Heinrich events” (HEs). Two competing models attempt to describe the stimulus for HEs via either internal ice sheet oscillations or external ocean-climate system forcing. We present a terrestrial record of HEs from the northeastern LIS that strongly supports ocean-climate forcing. Subglacial carbonate precipitates from Baffin Island record episodes of subglacial melting coincident with the three most recent HEs, resulting from acceleration of nearby marine-terminating ice streams. Synchronized ice stream acceleration over Baffin Island and Hudson Strait is inconsistent with internal ice sheet oscillations alone and indicates a shared ocean-climate stimulus to coordinate these different glaciological systems. Isotopic compositions of these precipitates record widespread subglacial groundwater connectivity beneath

the LIS. Extensive basal melting and flushing of these aquifers during the last HE may have been a harbinger for terminal deglaciation.

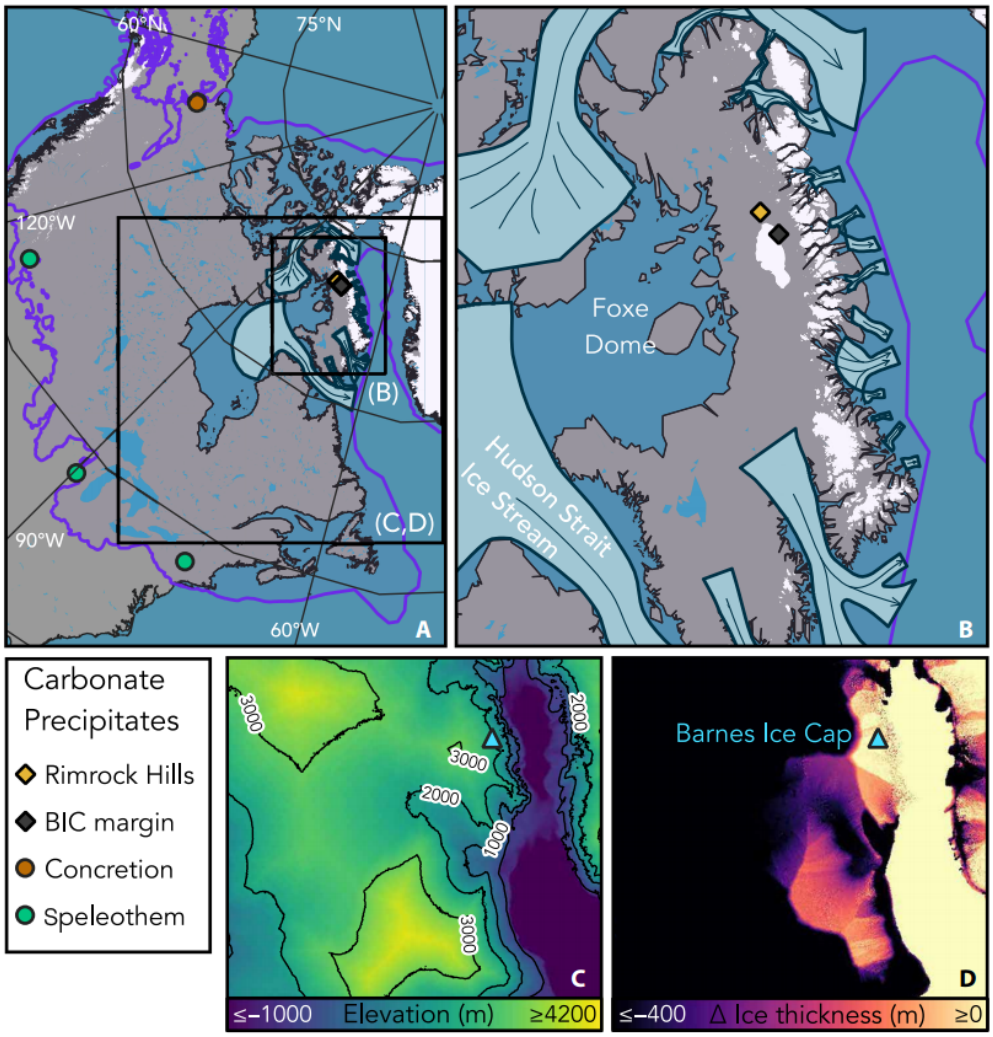

Figure 1. Modern and LGM conditions of northern North America and Baffin Island. (A and B) Modern sea level and land-ice distribution (white) are overlain by LGM Laurentide Ice Sheet extent (purple border) (*73*), paleo-ice streams draining the Foxe Dome (pale blue with dark borders) (*33*), subglacial carbonate precipitates measured in this study (diamonds), and groundwater-fed periglacial carbonate precipitates with δ234Uo >500‰ (circles) (*47*, *58–60*). Black boxes in (A) indicate extents of (B) to (D). (C) Reconstructed ice surface elevation and surrounding land and bathymetry (relative to modern sea level) at 20 ka ago (*35*). (D) Change in reconstructed ice thickness between 20 and 12.5 ka ago (*35*).

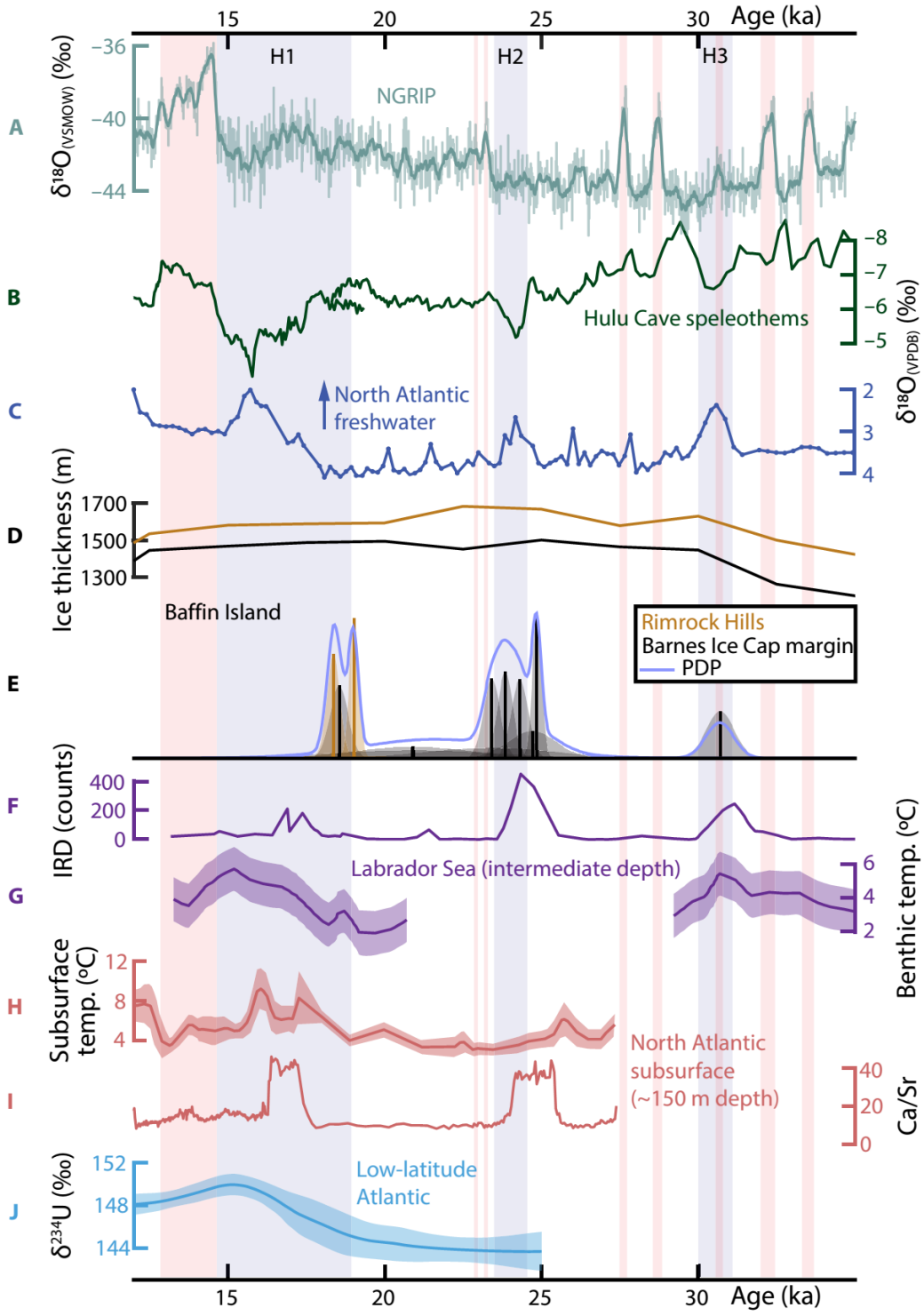

Figure 2. Chronologic comparison of Baffin Island subglacial calcite-forming events with various climate, ocean, and ice sheet records. Datum: 1950 CE. Proxies from the same record share the same color. Pale red bars indicate "Greenland Interstadial" events (75). Pale blue bars indicate HEs: H1 spans the comprehensive time frame of (17) and H2 and H3 span associated excursions in the Hulu Cave speleothem record (B). (A) NGRIP $\delta^{18}O$ record of Greenland temperature variation (GICC05

time scale, adjusted to 1950 CE datum) (75). (B) $\delta^{18}O$ of Hulu Cave stalagmites (PD and MSD) record Asian monsoon precipitation changes that vary synchronously with Greenland temperature changes (5). (C) Sinistral Neogloboquadrina pachyderma $\delta^{18}O$ record at Orphan Knoll (core MD95-2024P), a proxy for freshwater flux into the North Atlantic (27, 28). (D) Reconstructed ice thickness over the Rimrock Hills and Barnes Ice Cap margin (35). (E) Dates of Baffin Island calcite-forming events from this study and (22), traced with a probability density plot (PDP) calculated using (76). Bells indicate uncertainty distributions of the means (vertical lines) and heights scale with precision (only relative heights matter, absolute values omitted). (F) Carbonate ice-rafted detritus (IRD) and (G) water temperatures calculated from benthic foraminifera Mg/Ca (±1 analytical uncertainty) at an intermediate-depth site in the Labrador Sea (core EW9302-2JPC) (10). (H) North Atlantic subsurface (~150 m depth) water temperatures calculated from Mg/Ca ratios of sinistral N. pachyderma (envelope denotes 95% confidence interval) and (I) bulk sediment Ca/Sr, a proxy for carbonate IRD (core GeoB18530-1) (14). (J) Seawater $\delta^{234}U$ (±2 uncertainty) in the upper (<1.5 km depth) low-latitude North Atlantic Ocean, reconstructed from deep-sea corals (19).

2. 马尼拉北部俯冲带的地壳结构:吕宋弧和弧前之下俯冲的是减薄的陆壳还是洋壳？

翻译人：刘伟 inewway@163.com

Liu S, Gao J, Zhao M, et al. ***Crustal structure of the northern Manila subduction zone: Is thinned continental crust or oceanic crust subducting beneath the Luzon arc and forearc****?[J].* ***Tectonophysics****, 2022, 844: 229605.*

https://doi.org/10.1016/j.tecto.2022.229605

摘要：横贯南海东北缘和马尼拉俯冲带（21°N）东西向 280 km 广角反射/折射剖面的 p 波正演-反演速度模型揭示了位于马尼拉平移断层(MTF)和马尼拉板片以西的 10-12 km 厚的减薄陆壳(TCC)。TCC 被大陆内速度差异边界(VDB)划分为两个部分。在 VDB 以西，TCC 位于一个高速层(HVL)之上。在 VDB 以东，TCC 顶部发育一套速度异常体（Undefined Body），位于增生楔底部，与拆离断层相连，东部被马尼拉平移断层（MTF）切断。地震的分布表明，自吕宋弧与欧亚大陆在约 7 Ma 发生碰撞以来，约 80 公里的地壳已经在马尼拉平移断层以东俯冲。所有已发表的层析成像都表明了洋壳的俯冲作用。然而，由于地壳校正，马尼拉板片的上部可能最终存在一个最大宽度达 40 公里的减薄陆壳，而不是洋壳。在~ 7 Ma 时，马尼拉板片的上部恢复了两种可能的 40 公里宽的地壳端元（陆壳或洋壳）。从那时起，北吕宋岛向西北方向移动了约 600 公里，部分移动被欧亚大陆薄陆壳的收缩吸收到恒春半岛附近，导致马尼拉板片和马尼拉平移断层顺时针旋转了约 20°。吕宋岛弧微块体开始顺时针旋转 10°-30°，其中在台湾北部发生旋转的时间在 7 Ma，在海岸山脉为 3-4 Ma，在鹿涛和兰屿岛为 1 Ma，而在恒春半岛以南不旋转。因此，无论是单个吕宋弧块的顺时针旋转，还是马尼拉板片和马尼拉平移断层的顺时针旋转，都可以解释吕宋弧与欧亚大陆的碰撞过程。

ABSTRACT: Forward and inverse P-wave velocity models along an E-W 280-km-long wide-angle reflection/refraction profile at 21°N across the northeastern South China Sea margin and Manila subduction zone reveal a 10–12 km thick thinned continental crust (TCC) located west of the Manila transcurrent fault (MTF) and Manila slab. The TCC is divided in two parts separated by the intra-continental velocity difference boundary (VDB). West of the VDB, the TCC is located above a high

velocity layer (HVL). East of the VDB, the TCC consists of three layers: an undefined body with a velocity inversion at its base above the upper and lower crusts. The VDB and MTF merge east of the Hengchun peninsula showing that the TCC located east of the VDB decreases in size and disappears to the north. The distribution of earthquakes (EQs) shows that ~80 km of crust have subducted east of the MTF since the onset of Luzon arc collision with Eurasia at ~7 Ma. All published tomographies suggest the subduction of oceanic crust (OC). However, due to crustal corrections, up to a maximum width of 40 km of TCC might eventually exist in the upper part of the Manila slab instead of OC. Two end-members with 40 km of TCC or not in the upper part of the Manila slab were restored at ~7 Ma. Since that time, the north Luzon island moved ~600 km in the northwest while part of this motion was absorbed near the Hengchun peninsula by shrinking of Eurasia TCC, resulting in a ~ 20° clockwise rotation of the Manila slab and MTF. Small Luzon arc blocks started to rotate 10°-30° clockwise at ~7 Ma below northern Taiwan, 3–4 Ma in the Coastal range and 1 Ma in Lutao and Lanyu islands and not south of the Hengchun peninsula. Thus, both the clockwise rotation of the individual Luzon arc blocks and of the Manila slab and MTF might explain the collision process of the Luzon arc with the Eurasia continent.

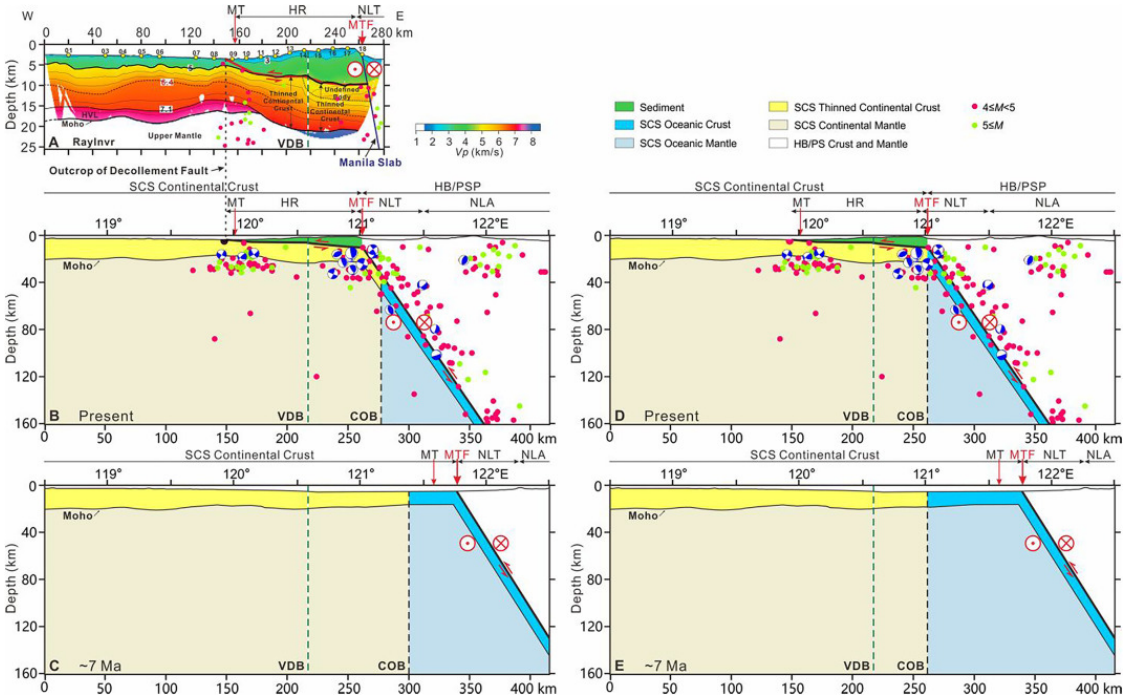

Figure 1. Interpretation of the wide-angle seismic Profile OBS2015–2_OBS2016–1 replaced in the general context of the Manila subduction zone (No vertical exaggeration). (A) RayInvr model of Profile OBS2015–2_OBS2016–1 with earthquakes (EQs) of magnitude >4 from the International Seismological

Centre (ISC) database in a 30-km wide stripe along the profile. (B) General context of the Manila subduction zone in the global convergent system with the same EQs as in A. End member with 40 km of thinned continental crust already subsided. (C) Corresponding geodynamic context of the Manila subduction zone ~7 Ma ago. (D) General context of the Manila subduction zone in the global convergent system with the same EQs as in A. End member with no subsided thinned continental crust. (E) Corresponding geodynamic context of the Manila subduction zone ~7 Ma ago. Sediment layer in green. The blue and white balls are focal-mechanism solutions. In C and E, the Hengchun accretionary wedge was reduced in size and not drawn, the Manila trench was ~20 km west of the MTF, and the Manila slab and the Huatung basin-Philippine Sea plate (HB-PSP in white) were located ~80 km east of their present-day location. Thinned continental crust in yellow and oceanic crust in blue. Continental mantle in light yellow and oceanic mantle in light blue. COB, continent-ocean boundary; HR, Hengchun ridge; MT, Manila trench; NLA, north Luzon arc; NLT, north Luzon trough; VDB, intra-continental velocity difference boundary.

3. 碎屑含量较高的石笋可用古地磁方法定年

翻译人：杨会会 11849590@mail.sustech.edu.cn

Sanchez-Moreno E. M., Font E., Pavón-Carrasco F. J., et al., ***Paleomagnetic techniques can date speleothems with high concentrations of detrital material[J].*** *Scientific Reports. 2022;12:17936.*

https://doi.org/10.1038/s41598-022-21761-9

摘要：由于难以评估碎屑污染物的同位素组成和在原位产生的 ^{230}Th 的低丰度，使得年轻和“脏”的石笋，难以采用 U 系定年法进行定年。在此，我们提出了一种基于石笋古地磁方向与全球古地磁重建参考曲线对比的新测年方法。从葡萄牙中部地区的 Soprador do Carvalho 洞穴收集的石笋证明了这种方法。利用 4 个 U 系列年龄和 3 个 ^{14}C 年龄建立的放射性同位素年龄模型表明，从公元前 5760 年到公元 1920 年，碳酸盐沉积相对稳定。我们对 45 个 6 mm 厚的子样品使用交变场和热退磁法进行分析，提供了明确的主要磁方向。将石笋的古地磁记录与以往的古地磁长期变化曲线（重建模型得到的参考曲线）进行拟合，并应用“解靴法”统计法确定最佳拟合，得到的石笋年龄模型与放射性同位素年龄模型拟合较好，但具有较高的时间分辨率。当我们将这种方法应用于另一种来自葡萄牙阿尔加维地区的石笋时，我们得到了同样的结论。因此，我们的方法似乎是对碎屑含量较高的年轻石笋进行定年的有效替代方法。

ABSTRACT: The U-series dating of young and ‘dirty’ speleothems is challenging due to difficulties in assessing the isotopic composition of detrital contaminants and the low-abundance of ^{230}Th generated in situ. Here we propose a new dating approach based on the comparison of a speleothem’s paleomagnetic directions to reference curves from global paleomagnetic reconstructions. This approach is demonstrated on a stalagmite collected from the Soprador do Carvalho cave in the Central Region of Portugal. A radio isotopic age model, built using four U-series ages and three ^{14}C, suggests relatively steady carbonate precipitation from ~ 5760 BCE until ~ 1920 CE. Forty-five 6 mm-thick subsamples were analyzed using alternating field and thermal demagnetization protocols, providing well-defined, primary magnetic directions. An age

model of the stalagmite was obtained by fitting its paleomagnetic record with the reference paleosecular variation curves obtained by previous paleo-reconstruction models, applying statistical bootstrapping analysis to define their best fit. The resulting age models fit closely with the radio isotopic age model but provide a significantly higher time resolution. We reach the same conclusion when applying this approach to another stalagmite from the Algarve region of Portugal. Our approach thus appears a promising alternative to date young speleothems with high detrital contents.

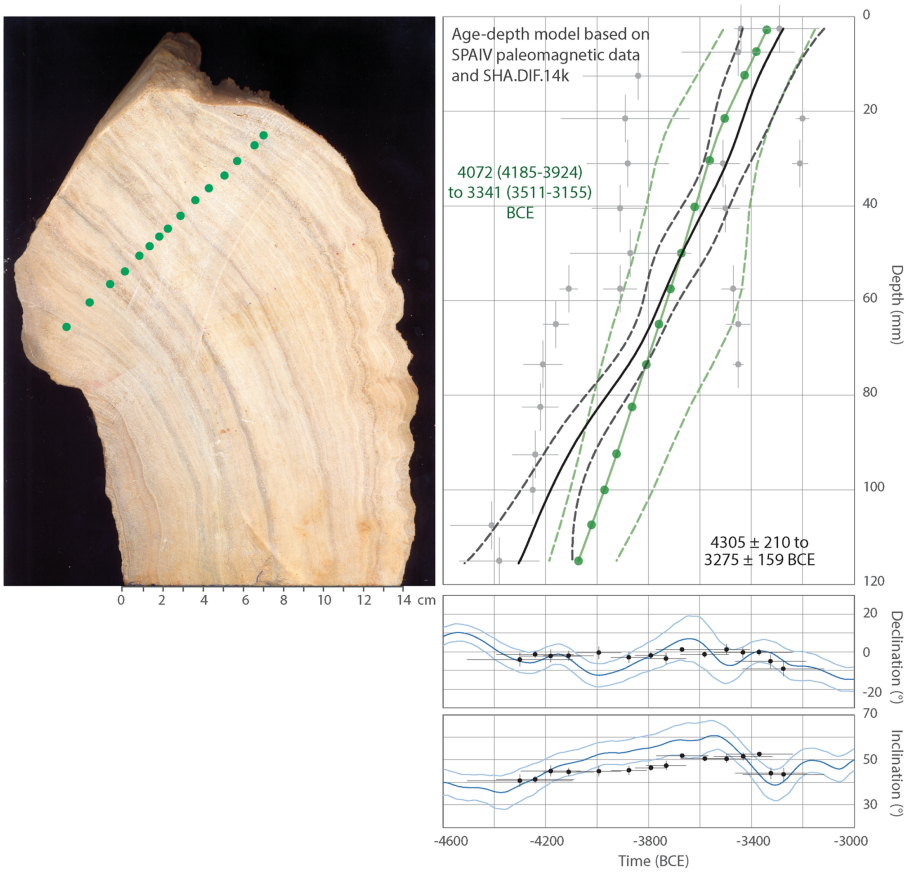

Figure 1. The age-depth model of the Algarve speleothem obtained by fitting the paleomagnetic data to the PSV curve from the SHA.DIF.14k model, using our statistical bootstrapping analysis (in black). Age-depth model based on interpolated U-series ages (in green). Below is the position of the paleomagnetic data on the PSV curve after fitting. See Fig. 4 for legend. Green points in the speleothem picture represent the sample-based mean directions calculated by Ref.26 in 15 calcite laminae for which ages were calculated based on U-series isochrons using the StalAge algorithm. All data errors and error bands are shown at 95% of probability.

4. 地磁日变揭示的相对干燥的地幔过渡带

翻译人：曹伟 11930854@qq.com

Zhang H, Egbert G, Huang Q. ***A relatively dry mantle transition zone revealed by geomagnetic diurnal variations*** *[J]* ***Science Advances****, 2022, 8, eabo3293.*

https://doi.org/10.1093/gji/ggab257

摘要：地幔过渡带（MTZ）内的水分布对地幔物质循环和部分熔融具有重要意义。虽然氢的溶解度非常高，导致人们猜测 MTZ 在深地水循环中起着关键作用，但实际水含量仍然是一个悬而未决的问题。地幔矿物的电导率对含水量非常敏感，因此对 MTZ 中这一物理参数的可靠估计将提供有价值的约束。本文利用新近开发的地磁日变联合反演方法，得到了真实的地磁源结构和一维地幔电导率剖面。综合试验表明，在模型分辨率最好的深度（200 至 600 千米）上，得到的剖面是大陆地幔导电性分布的合理指标，即使存在横向非均质性。推论 MTZ 中的水浓度为 0.03％（重量），比 wadsleyite 和 ringwoodite 的溶解度低一到两个数量级。

ABSTRACT: The distribution of water within the mantle transition zone (MTZ) has important implications for the material circulation and partial melting of the mantle. Although solubility of hydrogen is very high, leading to speculations that the MTZ plays a key role in the deep-Earth water cycle, the actual water content remains an open question. Electrical conductivity of mantle minerals is very sensitive to water content, so reliable estimates of this physical parameter in the MTZ would provide valuable constraints. Here, we use recently developed joint inversion of geomagnetic diurnal variation for realistic source structure and one-dimensional mantle conductivity profile. Synthetic tests show that the resulting profile is a reasonable proxy for the electrical conductivity distribution of continental mantle over depths where model resolution is best (200 to 600 kilometer), even in the presence of lateral heterogeneity. The inferred water concentration in the MTZ is 0.03 weight %, one to two orders of magnitude below the solubility of wadsleyite and ringwoodite.

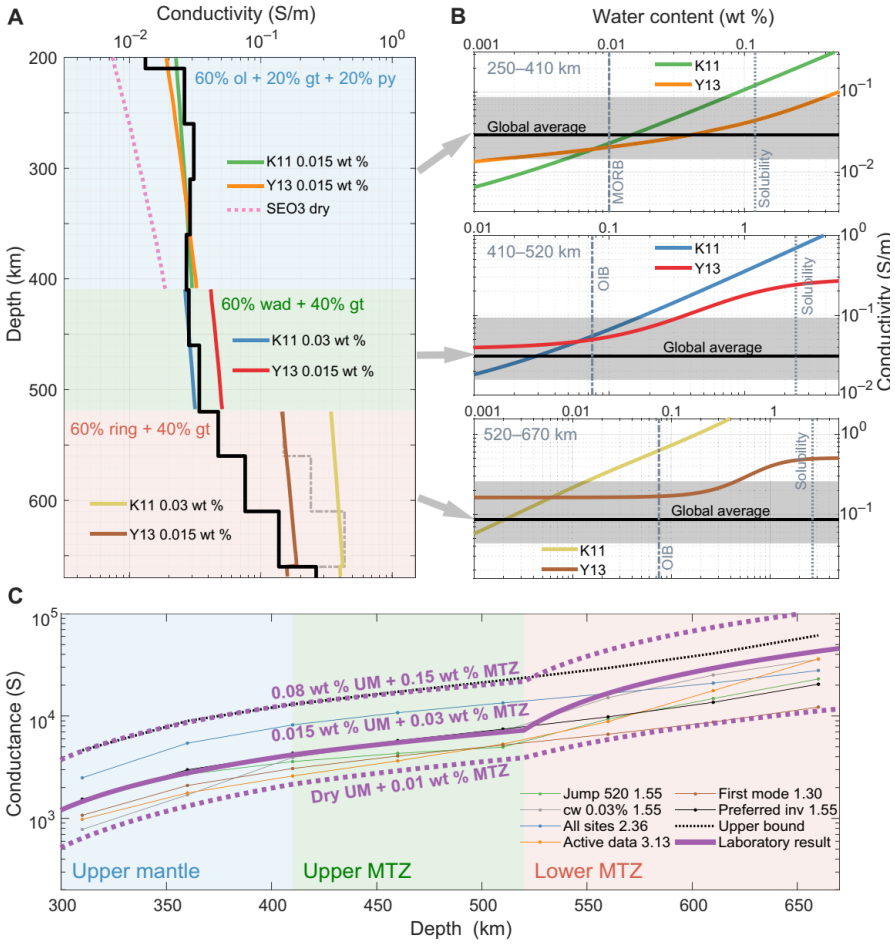

Figure 1. Water content in the upper mantle and MTZ. (A) Conductivity-depth profile (black line), compared to laboratory-based profiles derived from mineral physics experiments on nominally anhydrous minerals with hydrogen using adiabatic mantle temperature profile. The pink dot-dashed line is the dry peridotite model SEO3 with quartz-fayalite-magnetite buffer. (B) Layer averaged bulk conductivity of minerals aggregate as a function of bulk water content and the averaged conductivity derived from preferred inversion profile (black line) with uncertainty (gray). From top to bottom: the upper mantle, upper MTZ, and lower MTZ. MORB, mid-ocean ridge basalt; OIB, ocean island basalt. (C) Conductance-depth profile of plausible inverted models derived from various data and inversion schemes. The black dotted line denotes the upper bound of conductance derived from preferred conductivity profile, accounting for estimated uncertainty. The thick purple lines denote calculated conductance based on laboratory studies with fixed water contents in upper mantle and MTZ: Solid line corresponds to best match to preferred conductivity profile, and dotted lines represent upper and lower bounds. For the lower bounds, both the upper mantle and lower MTZ are dry (0.001 wt % water). Olivine, ol; wadsleyite, wad; ringwoodite, ring; garnet, gt; and pyroxene,

py; UM, upper mantle.

5. 地核内湍流磁扩散的证据

翻译人：张伟杰 12031188@mail.sustech.edu.cn

Holdenried‐Chernoff D, Buffett B A. Evidence for Turbulent Magnetic Diffusion in Earth's Core[J]. Geochemistry, Geophysics, Geosystems, e2022GC010672.

https://doi.org/10.1029/2022GC010672

摘要: 根据目前对外核分子磁扩散率的估计，古磁场的波动表明偶极子衰变时间比预期的短。在湍流发电机模拟中也观察到类似的行为，其短的磁场衰减时间不能归因于高阶衰减模式。我们将短的衰减时间解释为湍流扩散，并表明平均场理论可以定量解释发电机的结果。预测取决于与磁场相互作用的流体的振幅和长度规模。我们依靠洛伦兹/科氏力和浮力/科氏力之间的两两平衡来识别相关部分的流动，并使用由此产生的流动特性来再现在不确定性范围内的数值发电机模拟结果。将这些预测扩展到古磁场，我们发现推断的衰减时间需要体积均方根速度小于 0.8-1.2 mm s^{-1}。根据对长期变化的观察，之前地核顶部估计的速度略低。这些结果表明，地核内部的速度可以通过古地磁观测来约束，同时这种流动的幅度不能远远超过来自地核表面的估计。

ABSTRACT: Fluctuations in the paleomagnetic field suggest that the dipole decay time is shorter than expected, based on current estimates for the molecular magnetic diffusivity in the outer core. Similar behavior is observed in turbulent dynamo simulations, where the short magnetic field decay time cannot be attributed to higher-order decay modes. We interpret the short decay time as a signature of turbulent diffusion and show that mean-field theory can quantitatively account for the dynamo results. The predictions depend on the amplitude and length scale of the flow that interacts with the magnetic field. We rely on the pairwise balance between Lorentz/Coriolis and buoyancy/Coriolis forces to identify the relevant part of the flow, and use the resulting flow properties to reproduce results from numerical dynamo simulations within their uncertainties. Upon extending these predictions to the paleomagnetic field, we find that the inferred decay time requires a bulk root-mean-square velocity less than 0.8 to 1.2 mm s^{-1}. Somewhat lower velocities have been

estimated at the top of the core from observations of secular variation. These results show that velocities in the interior of the core are constrained by paleomagnetic observations, and that the amplitude of this flow cannot substantially exceed estimates at the core surface.

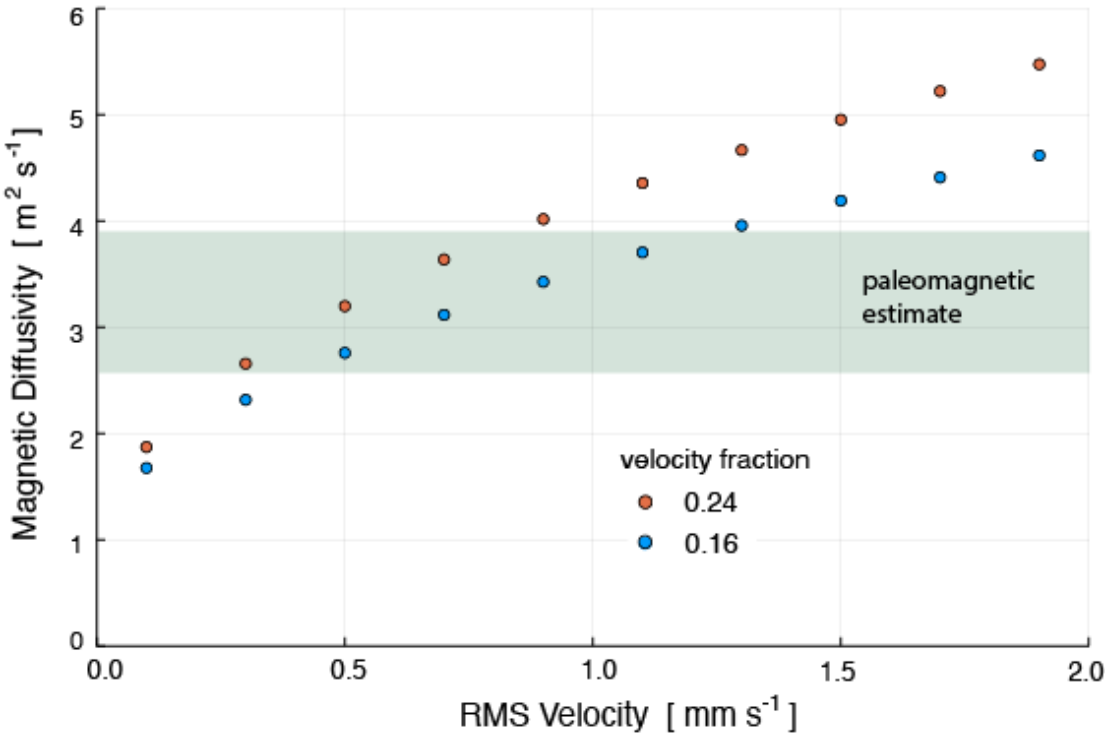

Figure 1. Total magnetic diffusivity as a function of the rms fiuid velocity U_{rms}.

6. 陆地气候变化在千年尺度上被海洋温度变化覆盖

翻译人：李海 12031330@mail.sustech.edu.cn

Hébert R, Herzschuh U, Laepple T. ***Millennial-scale climate variability over land overprinted by ocean temperature fluctuations*** *[J]. Nature Geoscience, 2022.*

https://doi.org/10.1038/s41561-022-01056-4

摘要：区域温度变化对社会具有广泛的影响，但我们对长期自然变化的幅度和机理的理解不足以准确的预测区域变化。地球温度的变化尤其如此，目前认为地球温度在长时间尺度上的变化是微弱的。通过对重建的古气候记录进行功率谱分析，利用北半球 8000 年以来孢粉记录并结合观测资料，作者建立了年际至千年尺度的区域温度变化。结果表明短尺度随机变化在几十年甚至更长的时间尺度上被海洋气候的影响。与气候模型预测的相对温暖和一致的变暖相比，这可能会对下个世纪区域气候变化造成很大影响。由于海洋的影响，在亚年代际时间尺度上，以稳定海洋气候特征的区域会经历更强的长期变化，而大陆区域则表现为较弱的长期变化。时间尺度之间的这种关系对海洋驱动低频气候变化机制提供了独到的见解，并为预测几十年至更长时间尺度的温度波动幅度奠定了基础。

ABSTRACT: Variations in regional temperature have widespread implications for society, but our understanding of the amplitude and origin of long-term natural variability is insufficient for accurate regional projections. This is especially the case for terrestrial temperature variability, which is currently thought to be weak over long timescales. By performing spectral analysis on climate reconstructions, produced using sedimentary pollen records from the Northern Hemisphere over the last 8,000 years, coupled with instrumental data, we provide a comprehensive estimate of regional temperature variability from annual to millennial timescales. We show that short-term random variations are overprinted by strong ocean-driven climate variability on multi-decadal and longer timescales. This may cause substantial and potentially unpredictable regional climatic shifts in the coming century, in contrast to the relatively muted and homogeneous warming projected by climate models. Due to the marine influence, regions characterized by stable oceanic climate at sub-decadal timescales experience stronger long-term variability, and continental regions with higher sub-

decadal variability show weaker long-term variability. This fundamental relationship between the timescales provides a unique insight into the emergence of a marine-driven low-frequency regime governing terrestrial climate variability and sets the basis to project the amplitude of temperature fluctuations on multi-decadal timescales and longer.

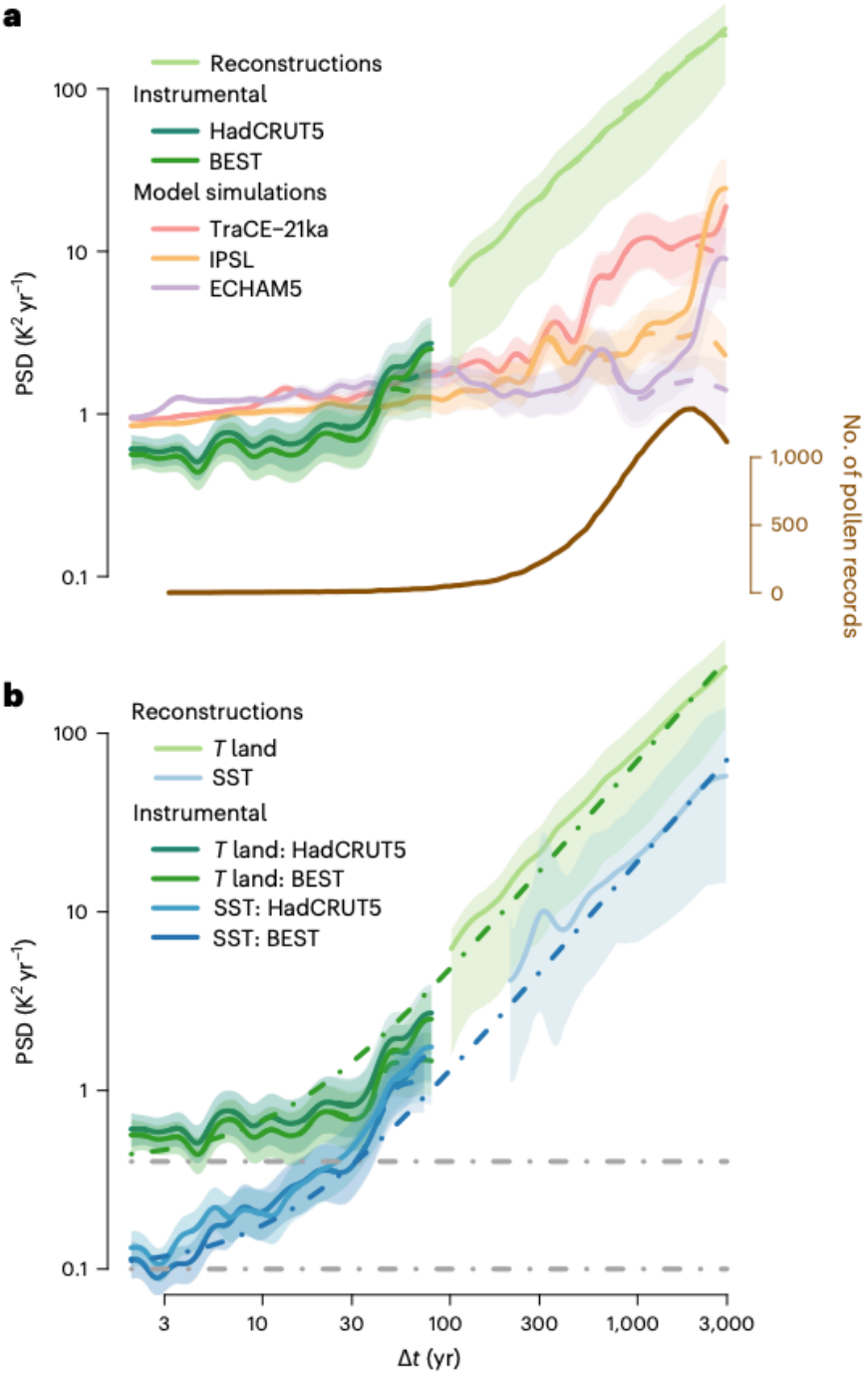

Figure 1. a, PSD estimates of land air temperature (T land) from pollen-based reconstructions along instrumental data and model simulations, both extracted at the pollen record locations;

logarithmically spaced axes were used. Also shown are estimates from timeseries detrended with a 23-kyr sinusoidal or with respect to log(CO_2) (dashed). The number of pollen records contributing to each timescale is indicated below (brown axis). b, Average spectral estimates from reconstructed annual SSTs, and instrumental data at the corresponding locations. Observational spectra from a are reproduced. Linear combinations of power laws with slope $\beta = 1.2$ and white-noise series are shown as dashed-dotted lines (land in green, sea in blue and white-noise levels in grey). Shading indicates 90% confidence intervals around the mean.

7. 浮游有孔虫 Mg/Ca，团簇（Δ47）和稳定同位素（$\delta^{18}O$）在古海洋学温度研究中的组合应用

翻译人：张亚南 zhangyn3@mail.sustech.edu.cn

Peral M, Bassinot F, Daëron M, et al. ***On the combination of the planktonic foraminiferal Mg/Ca, clumped (Δ47) and conventional ($\delta^{18}O$) stable isotope paleothermometers in palaeoceanographic studies*** *[J] Geochimica et Cosmochimica Acta, 2022, 339: 22-34.*

https://doi.org/10.1016/j.gca.2022.10.030

摘要：假设有孔虫团簇同位素（Δ47）与海水盐度和 pH 无关，那么 Mg/Ca, $\delta^{18}O$ 和Δ47 的组合在理论上可以帮助我们理清温度，盐度/$\delta^{18}O_{sw}$ 和 pH 信号。文中，我们提出了一个新的现代 Mg/Ca-Δ47 数据集，该数据集来自不同的海洋盆地，包含了很大的温度范围（0.2-25.4℃）。这些测量的方式和针对的属种与 Peral 等（2018）进行Δ47 校准时使用的一致，允许 Mg/Ca 和Δ47 之间进行比较（不包括 2 种底栖有孔虫的数据点）。在对 Mg/Ca 温度进行盐度和 pH 校正后，这个古温度指标具有很好的一致性，表明有孔虫Δ47 可能不受盐度和 pH 的影响。然而，我们的研究结果表明，Δ47 温度指标的不确定性仍然限制了我们从 Mg/Ca，$\delta^{18}O$ 和 Δ47 组合中重建 pH 和 $\delta^{18}O_{sw}$ 的能力。我们也发现在修正生命，盐度和 pH 的影响后，*G. bulloides* 的 Mg/Ca 和Δ47 之间的差异依然存在，这表明其他过程也可能影响该物种的 Mg/Ca。本研究还提供了 Peral 等（2018）先前发表浮游和底栖有孔虫Δ47 校准的 I-CDES 更新版本，覆盖温度范围-2—25.4℃。

ABSTRACT: Assuming that foraminiferal clumped isotope (Δ47) values are independent of seawater salinity and pH, the combination of Mg/Ca, $\delta^{18}O$ and Δ47 values, may in theory allow us to disentangle the temperature, salinity/$\delta^{18}O_{sw}$ and pH signals. Here, we present a new Mg/Ca-Δ47 dataset for modern planktonic foraminifera, from various oceanographic basins and covering a large range of temperatures (from 0.2 to 25.4 °C). These measurements were performed on the same samples and species as the ones used for the foraminiferal Δ47 calibration of Peral et al. (2018), allowing comparison between both Mg/Ca and Δ47 paleothermometers (excluding the two benthic foraminiferal data points). There is a good agreement between these two paleothermometers when

the Mg/Ca-temperature is corrected for seawater salinity and pH, suggesting that foraminiferal Δ47 may not be influenced by salinity or pH. However, our results show that Δ47 temperature uncertainties still limit our ability to reconstruct pH and $\delta^{18}O_{sw}$ from the combination of Mg/Ca, $\delta^{18}O$ and Δ47 in a useful manner. We also find that disagreements between Mg/Ca and Δ47 values in *G. bulloides* persist after correction for vital, salinity and pH effects, suggesting that other process(es) may also influence Mg/Ca in this species.

This study also provides an updated I-CDES version of the previously published planktonic and benthic foraminiferal Δ47 calibration of Peral et al. (2018), covering a range of temperature from −2 to 25.4 °C.

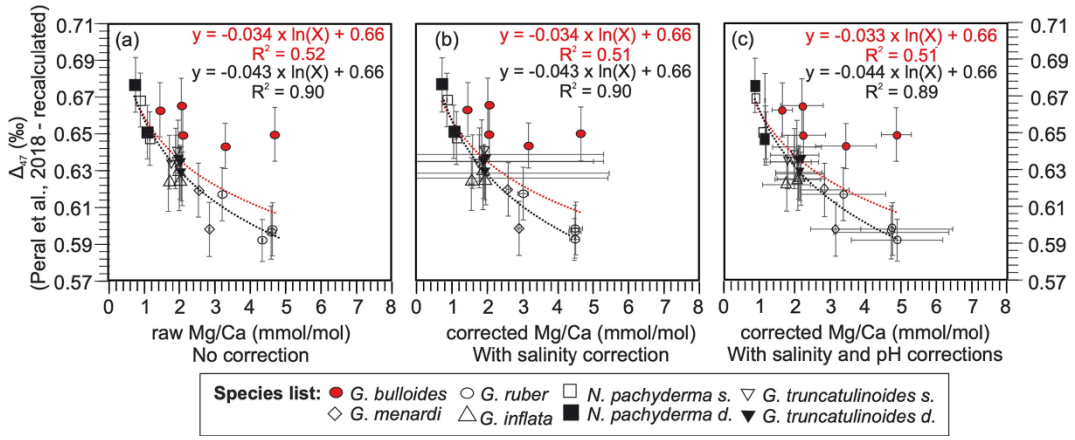

Figure 1. Comparison of our recalculated foraminiferal Δ47 values with raw Mg/Ca values (uncorrected) (a), with corrected Mg/Ca for salinity only (b), and with corrected Mg/Ca for salinity and pH (c). The Mg/Ca values are corrected using the equations from Gray and Evans (2019), the salinity and pH from the atlas and the oxygen isotopic temperatures. The red dotted logarithmic regressions are plotted for all the plots, including G. bulloides and the black regressions are without *G. bulloides*. All the uncertainties are at 2SE.

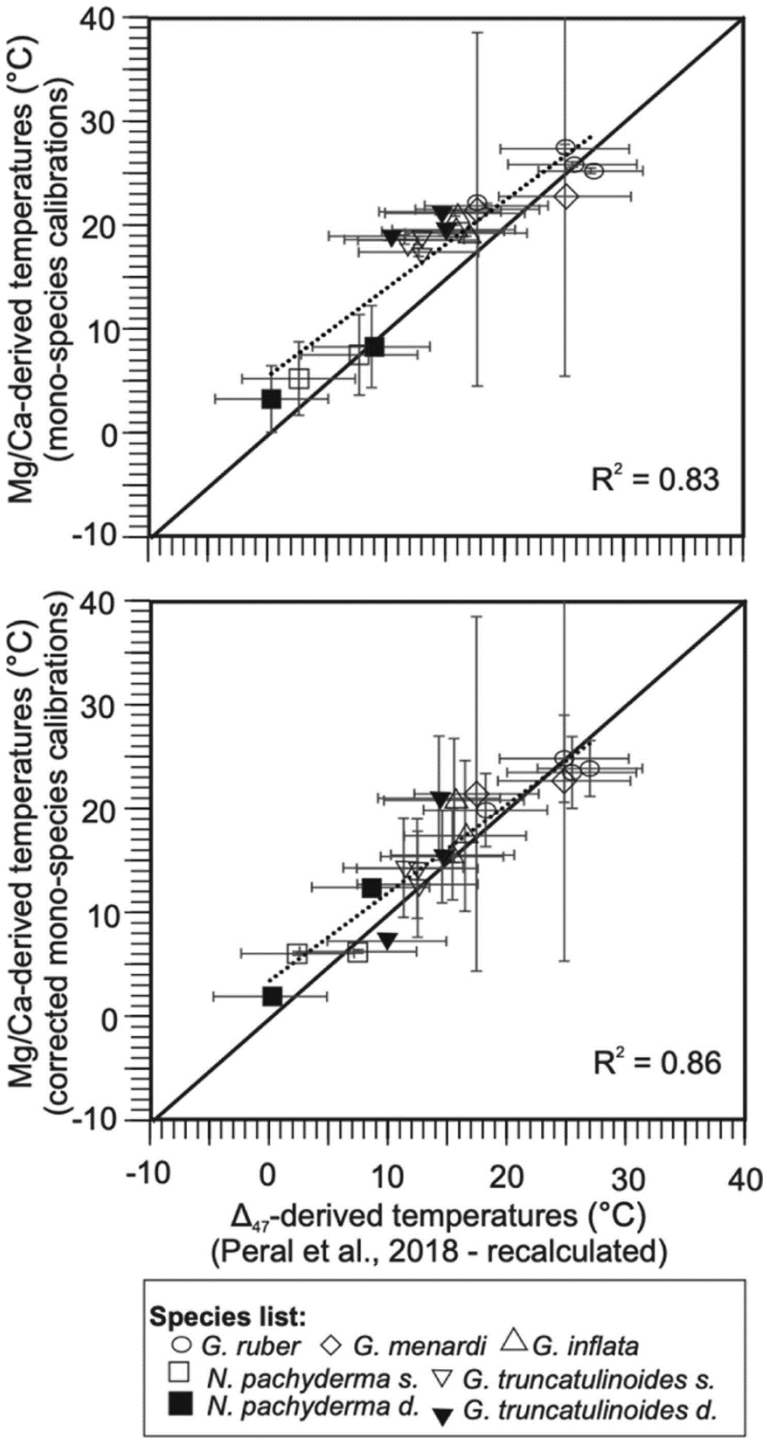

Figure 2. Mg/Ca-derived temperatures using mono-species calibrations, compared to the Δ47-derived temperatures using the recalculated Peral et al. (2018) calibration (a) and the Mg/Ca-derived temperatures using the corrected Mg/Ca mono-species calibrations for salinity and pH compared to the Δ47-derived temperatures using the recalculated Peral et al. (2018) calibration (b). The dotted linear regression, excluding *O. universa* and *G. bulloides*, is plotted. A line 1:1 is plotted in black; uncertainties are at 2 SE.

8. 全新世和末次间冰期期间绿色-沙漠撒哈拉转型的比较

翻译人：盖聪聪 gaicc@sustech.edu.cn

Li H, Renssen H, Roche D M. ***Comparison of the green-to-desert Sahara transitions between the Holocene and the last interglacial*** [J]. *Climate of the Past,* 2022, *18*, 2303-2319.

https://doi.org/10.5194/cp-18-2303-2022

摘要：“绿色撒哈拉”在末次间冰期（LIG）和全新世期间的荒漠化和植被反馈已得到广泛研究。然而，气候和植被变化的突然性及其相互作用仍在讨论中。本文应用中等复杂度的地球系统模型（iLOVECLIM）并结合两个动态植被模型（VECODE 和 LPJ-GUESS）来模拟全新世和 LIG 期间的气候—植被变化，进而比较北非植被的演变模式及其在这两个间冰期的反馈机制。本文结果证实 LIG 早期绿色撒哈拉的存在，这与全新世期间的绿色撒哈拉相似。结果显示，在这两个间冰期内，撒哈拉从植被丰富整体转变到沙漠化，但转变幅度相同。模拟的撒哈拉植被转变与 20°N 的夏季日辐射斜率呈线性相关，导致 LIG 期间植被覆盖的下降速度快于全新世。植被覆盖率减少的最大速率为 25%/kyr，发生在 122 ka。而在全新世期间，植被覆盖率减少的峰值为 10%/kyr，大约发生在 6 ka。在两次间冰期期间，表现为对气候的净植被正反馈。在早 LIG 和全新世期间，当植被覆盖率大于 60%时，植被通过植被—反照率反馈将降水增加 2 至 3 倍。由于 20°N 的夏季日辐射减少，植被覆盖随着大气进入的水分输送减少而减少，在两个间冰期造成夏季风的减弱。当正植被反照率反馈无法抵消夏季风减弱所导致的降水减少时，这种荒漠化会加速。植被正反馈对降水的影响随着植被盖度的降低而减小，而负植被—蒸发反馈的影响增加，加速了土壤水分和植被覆盖的流失。总体而言，在两个间冰期的早期阶段，植被的净正反馈很强，但由于 LIG 期间夏季日照的变化更快，LIG 期间植被的转变比全新世期间更突然。两个间冰期之间的主要区别在于降水变化率，在全新世期间降水变化率比 LIG 更慢，使得植被转变更缓慢。

ABSTRACT: The desertification and vegetation feedbacks of the “green Sahara” during the last interglacial (LIG) and the Holocene have been investigated by many studies. Yet the abruptness of climate and vegetation changes and their interactions are still under discussion. In this study, we

apply an Earth system model of intermediate complexity (iLOVECLIM) in combination with two dynamical vegetation models (VECODE and LPJ-GUESS) to simulate climate–vegetation changes during the Holocene and the LIG to compare the patterns of North African vegetation evolutions and mechanisms of their feedbacks during these two interglacials. Our results confirmed the existence of the green Sahara during the early LIG, which is as an analogue to the green Sahara during the Holocene. During both interglacials, an overall consistent transition from vegetated Sahara to desert is shown in our results, but the amplitudes of these transitions vary. These simulated Sahara vegetation transitions are nearly linearly related to the summer insolation declines at 20°N, resulting in faster declines of vegetation cover during the LIG than in the Holocene. The decline of vegetation cover peaks at 25% kyr^{-1} at around 122 ka, while during the Holocene the steepest vegetation cover decline is 10% kyr^{-1} at around 6 ka. Our results suggest net positive vegetation feedbacks to climate during the two interglacials. During the early LIG and Holocene, vegetation strengthens precipitation by a factor of 2 to 3 through the vegetation–albedo feedback when the vegetation cover is greater than 60%. Vegetation cover decreases with declines of the incoming moisture transport by the atmosphere due to the reduced summer insolation at 20◦ N, weakening the summer monsoon during both interglacials. This desertification is accelerated when the positive vegetation–albedo feedback cannot offset the reduction of precipitation due to a weaker summer monsoon. The impacts of this positive vegetation feedback on precipitation decrease with decreased vegetation cover, during which the impacts of negative vegetation–evaporation feedbacks increase, accelerating the loss of soil moisture and vegetation cover. Overall, the net positive vegetation feedback is strong during the early phases of both interglacials, but the vegetation transition is more abrupt during the LIG than during the Holocene due to the more rapid changes in summer insolation during the LIG. The main difference between the two interglacials is the rate of precipitation change, which is relatively gradual during the Holocene, leading to a more gradual vegetation transition in comparison to the LIG.

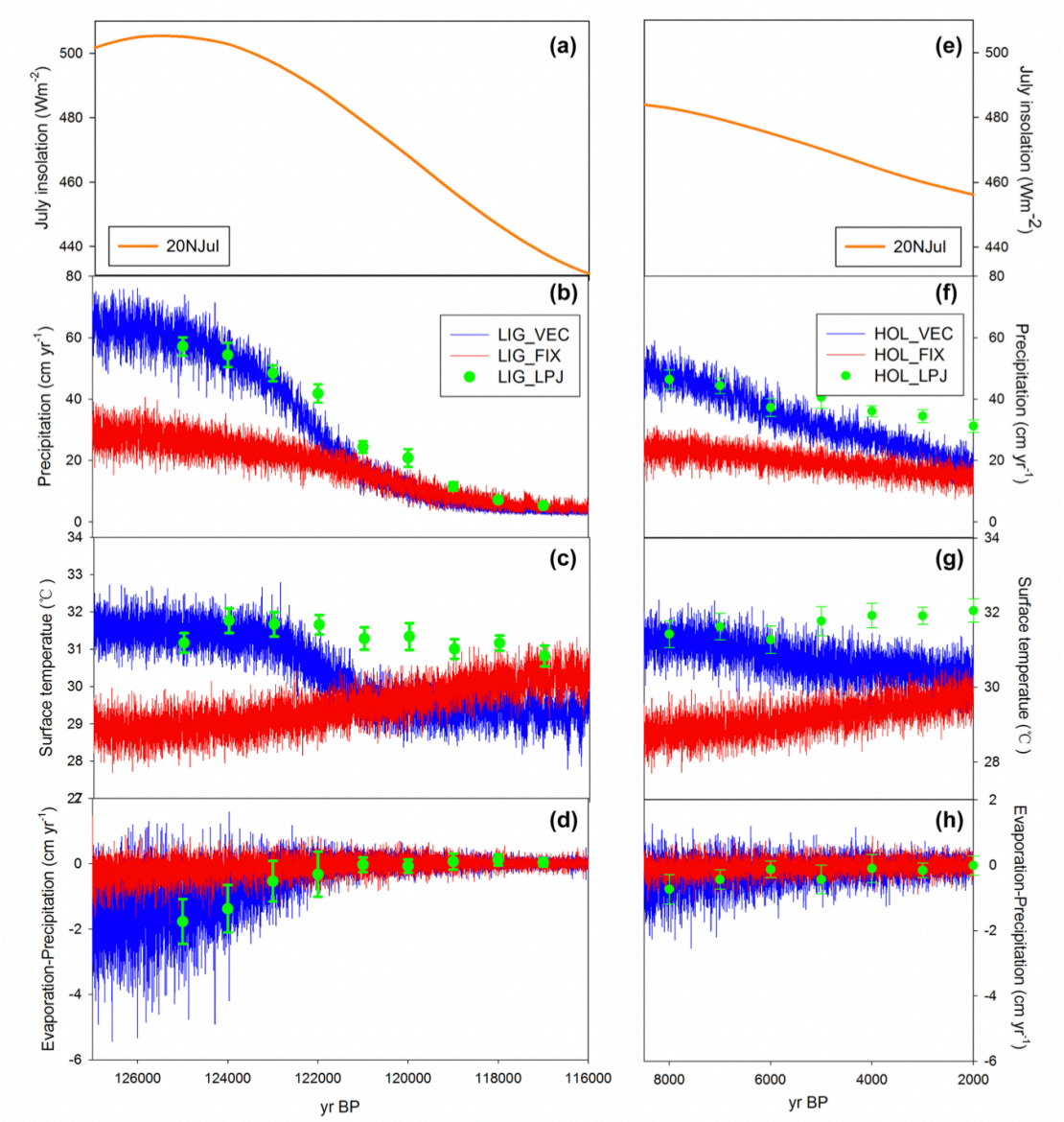

Figure 1. Evolution of 20°N July insolation, North African precipitation, surface temperature, and values of evaporation minus precipitation during the LIG (a, b, c, d) and Holocene (e, f, g, h). Our target area is delimited by 10°W to 35°E and 15 to 30°N. The blue lines and red lines are simulated results from transient experiments with dynamical vegetation and fixed pre-industrial vegetation, respectively. The green dots with error bars are simulated results from experiments with asynchronously coupled "dynamical" vegetation.

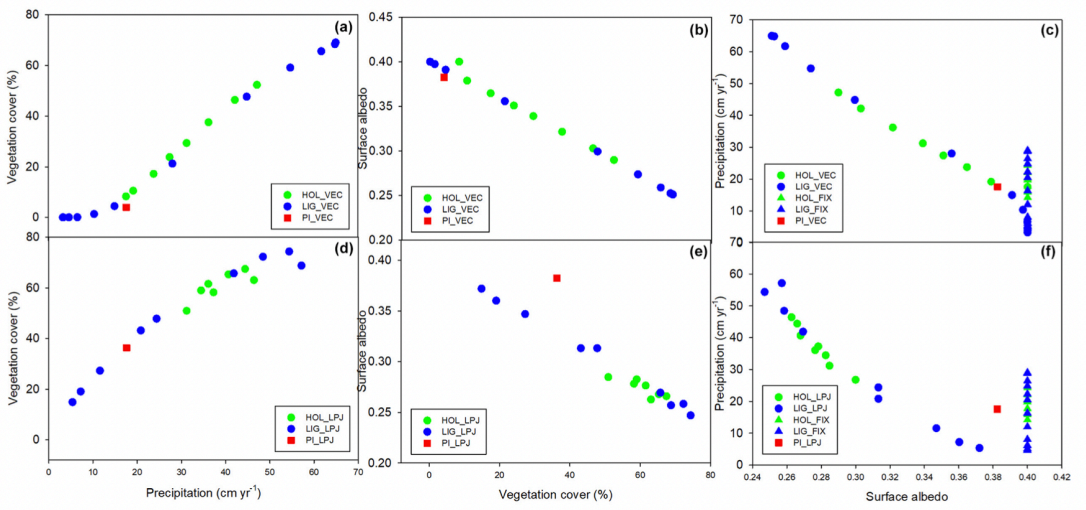

Figure 2. The relationship between (a) precipitation and vegetation cover; (b) vegetation cover and surface albedo; (c) surface albedo and precipitation with dynamical vegetation from VECODE during two interglacials; (d) precipitation and vegetation cover; (e) vegetation cover and surface albedo; (f) surface albedo and precipitation with dynamical vegetation from LPJ-GUESS during two interglacials.

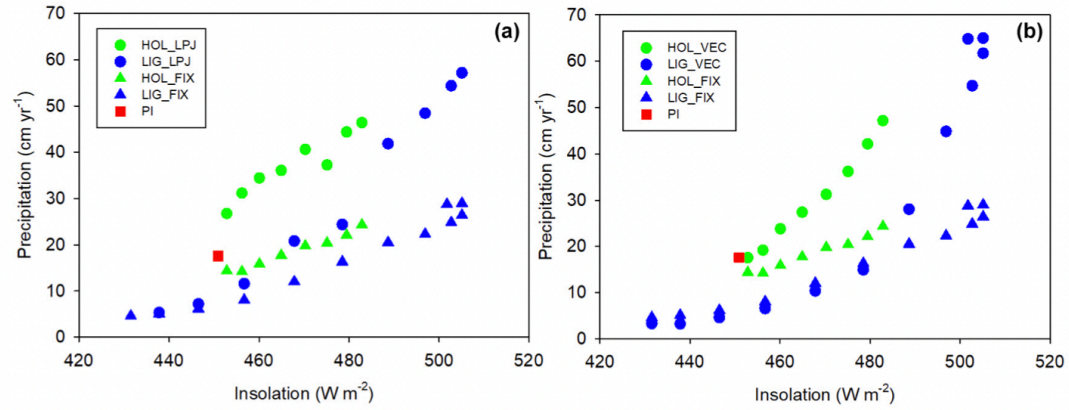

Figure 3. The relationship between insolation at 20°N and precipitation with dynamic vegetation from LPJ-GUESS (a) and VECODE (b) during two interglacials, with blue dots representing the LIG and green dots representing the Holocene. For reference, the results of HOL_FIX, LIG_FIX, and PI are also included.

9. 苏门答腊近海深海沉积物受浊积岩和生物扰动调节的胶黄铁矿的形成

翻译人：张琪 zhangq7@sustech.edu.cn

Yang T, Dekkers M, Zhao X, et al, ***Greigite formation modulated by turbidites and bioturbation in deep-sea sediments offshore Sumatra*** *[J]. Journal of Geophysical Research: Solid Earth, 2022, e2022JB024734.*

https://doi.org/10.1029/2022JB024734

摘要：沉积物中的自生胶黄铁矿可能形成于成岩作用过程中的任意时间。它的形成路径、时间和具有保存地质信息的潜力是鉴别含胶黄铁矿沉积物(古)地磁信号准确性的关键。在国际大洋发现计划 362 航次(苏门答腊俯冲边缘)岩心层序中，多个富含有机质的泥岩层位显示出较高的磁化率。高磁化率层位正好位于泥质浊积岩层顶生物扰动最严重的层位下方。对典型层位(海底以下约 1103.80-1108.80 米)沉积物的薄片和磁性矿物提取物进行矿物磁性、显微观测和化学分析，显示存在粗粒胶黄铁矿聚合物(颗粒大小可达 50-75 μm)。连续的浊积岩不稳状态导致了胶黄铁矿的形成。有机质、铁(氧)(氢)化物、Fe^{2+}、硫化物和硫酸盐在具有强烈的生物扰动层中富集。这也促使了胶黄铁矿的形成和保存，在随后的浊积岩脉冲形成的封闭成岩系统中，黄铁矿化由于缺乏铁(氧)(氢)化物的硫酸盐的供应不足而被阻止。以上可能代表了浊积岩和生物扰动调节下的一种新型胶黄铁矿形成方式。古磁学分析表明，早期成岩胶黄铁矿保留了原始的同期沉积磁性记录。极高的胶黄铁矿含量(0.06～1.30 wt%，由饱和磁化估算得到平均值为 0.50 wt%)表明生物扰动浊积沉积物是铁和硫的重要矿汇。因此，矿物磁学方法为更好地理解海洋 Fe-S-C 循环提供了一个新的视角。

ABSTRACT: Authigenic greigite may form at any time within a sediment during diagenesis. Its formation pathway, timing of formation, and geological preservation potential are key to resolving the fidelity of (paleo-)magnetic signals in greigite-bearing sediments. In the cored sequence of the International Ocean Discovery Program Expedition 362 (Sumatra Subduction Margin), multiple organic-rich mudstone horizons have high magnetic susceptibilities. The high-susceptibility horizons occur immediately below the most bioturbated intervals at the top of muddy turbidite beds.

Combined mineral magnetic, microscopic, and chemical analyses on both thin sections and magnetic mineral extracts of sediments from a typical interval (~1103.80–1108.80 meters below seafloor) reveal the presence of coarse-grained greigite aggregates (particles up to 50-75 μm in size). The greigite formed under non-steady-state conditions caused by the successive turbidites. Organic matter, iron (oxy)(hydr)oxides, Fe^{2+}, and sulfides and/or sulfate were enriched in these intensively bioturbated horizons. This facilitated greigite formation and preservation within a closed diagenetic system created by the ensuing turbidite pulse, where pyritization was arrested due to insufficient sulfate supply relative to Fe (oxy)(hydr)oxide. This may represent a novel greigite formation pathway under conditions modulated by turbidites and bioturbation. Paleomagnetic analyses indicate that the early diagenetic greigite preserves primary (quasi-)syn-sedimentary magnetic records. The extremely high greigite content (0.06–1.30 wt% with an average of 0.50 wt% estimated from their saturation magnetization) implies that the bioturbated turbiditic deposits are an important sink for iron and sulfur. Mineral magnetic methods, thus, may offer a window to better understand the marine Fe-S-C cycle.

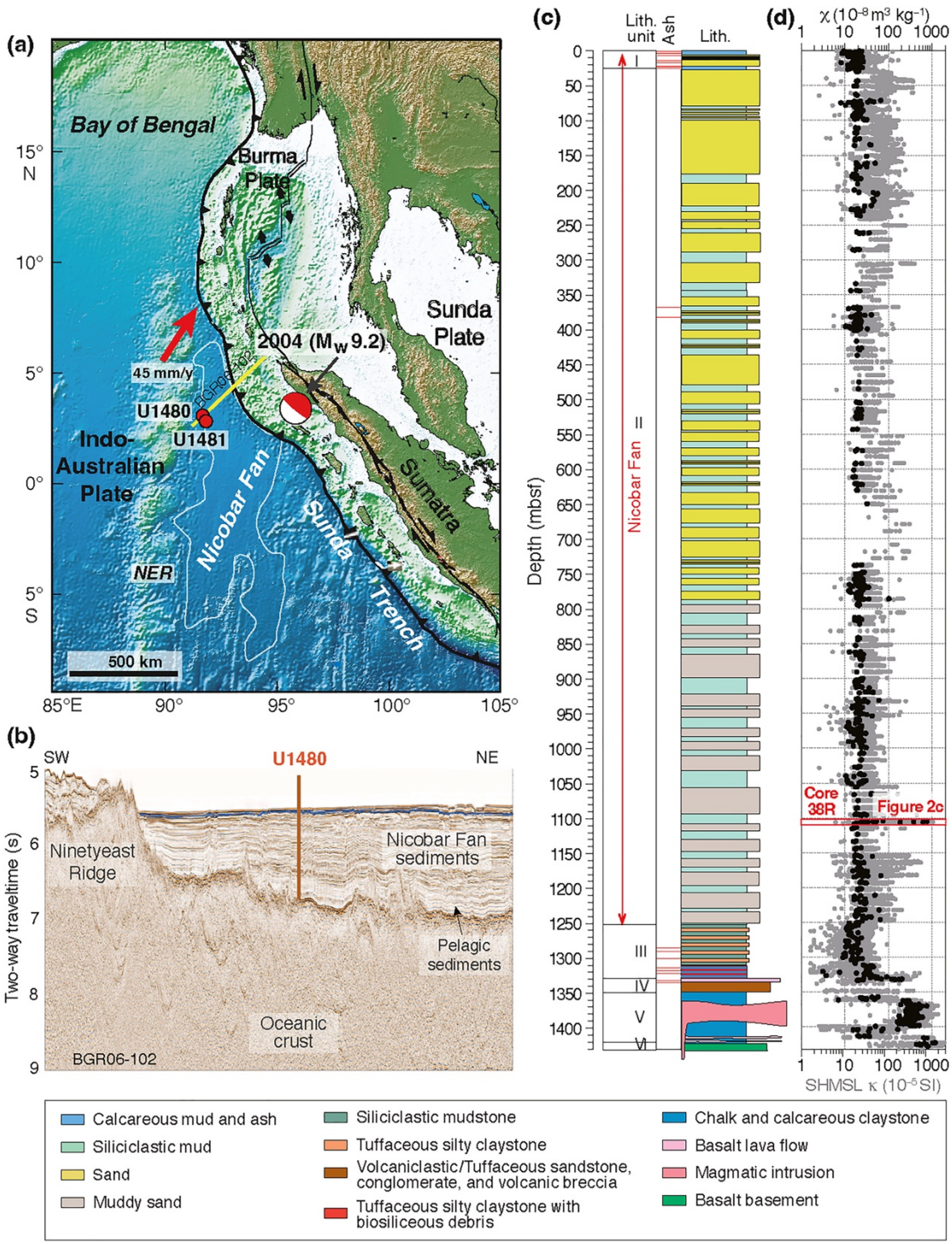

Figure 1. (a) Map of the north Sumatran subduction zone showing the location of drill sites U1480 and U1481 of IODP Expedition 362 (red dots), and the epicenter of the 2004 Mw 9.2 Sumatra - Andaman earthquake (focal mechanism symbol). Red arrow with number is a convergence vector (mm/year). NER, Ninety East Ridge. (b) Interpreted seismic profile BGR06-102 (indicated on Figure 1a) showing North Sumatran subduction input (i.e., Nicobar Fan sediments), with drill site U1480. (c) Lithostratigraphic units and subunits defined in Site U1480, mbsf = meters below sea

floor. (d) Downhole mass-specific magnetic susceptibility (χ) measured on discrete samples and magnetic susceptibility (SHMSL κ) measured with the SHMSL instrument on archive-half sections for Site U1480. A closeup view of the ~1103.8-1108.8 mbsf interval (Core 38R) is shown in Figure 2c.

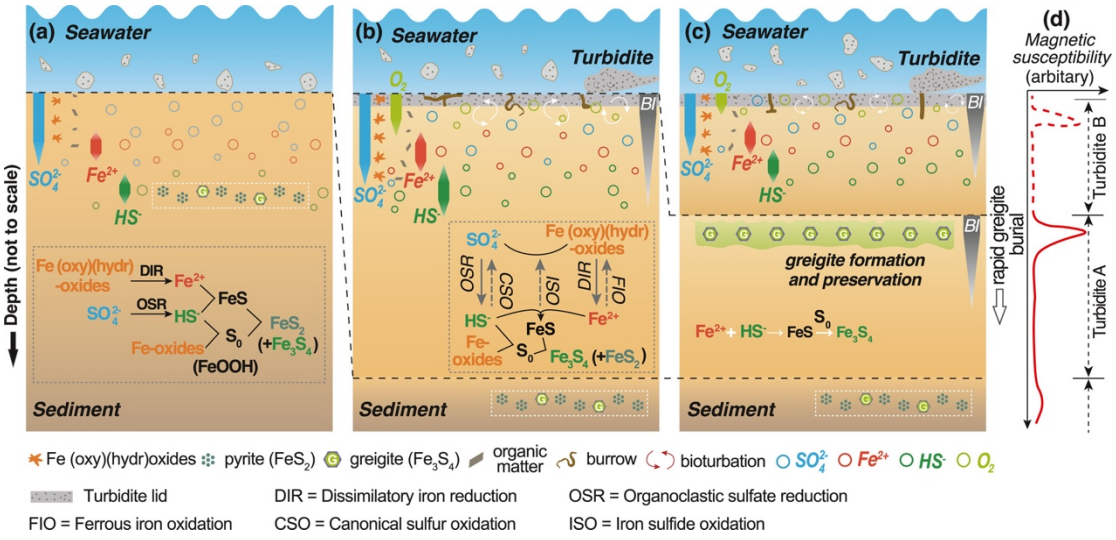

Figure 2. Conceptual model for the greigite-rich layers formation and preservation modulated by turbidites and bioturbation. (a) Under steady-state conditions in anoxic sediment, reductive dissolution of detrital iron (oxy)(hydr)oxide minerals releases dissolved Fe^{2+} into pore waters, where it reacts readily with upward diffusing hydrogen sulfide (HS^-) produced by organoclastic sulfate (SO_4^{2-}) reduction (OSR). This leads to iron monosulfide (FeS) precipitation, which subsequently reacts with sulfur (S_0) produced by direct reactions of iron oxides with HS^- to yield pyrite (FeS_2) with intermediate greigite (Fe_3S_4). Transformation of ferrimagnetic/antiferromagnetic iron (oxy)(hydr)oxides into paramagnetic pyrite results in a magnetic susceptibility decrease. (b) Deposition of organic-rich turbidites disrupts steady-state conditions. Intensive bioturbation causes downward transport of previously buried organic matter, iron (oxy)(hydr)oxides, and SO_4^{2-}. Upward diffusion of HS^- and Fe^{2+} in pore waters also occurs. Once in contact with O_2 at/near the sediment-water interface, they are (partially) reoxidized with formation of additional iron (oxy)(hydr)oxides and SO_4^{2-} respectively. These lead to enrichment of organic matter and iron (oxy)(hydr)oxides, Fe^{2+}, and HS^- and/or SO^{2-} at the top of the turbidite bed. (c) The ensuing mud-rich turbidite pulse 4 Accepted Article quickly buried the previous turbidite bed and creates closed system conditions. Rapid pore water SO^{2-} consumption via microbially mediated OSR leads to pore

water SO^{2-} depletion 44 and production of dissolved HS^{-}. Due to the relatively abundant reactants, plentiful Fe^{2+} and HS^{-} can be supplied to favor iron monosulfide (FeS) formation. Once supply of Fe^{2+} exceeds HS^{-}, the pyritization process is arrested and intermediate greigite is preserved. With successive turbidite pulses, multiple greigite-rich layers form in intensely bioturbated horizons at the tops of turbidite beds, resulting in multiple sedimentary magnetic susceptibility spikes (d).

10. 冰川气候突变期间巴芬湾和拉布拉多海的海冰波动

翻译人：夏文月 12231072@mail.sustech.edu.cn

Scoto F., Sadatzki H., Maffezzoli N O., et al. ***Sea ice fluctuations in the Baffin Bay and the Labrador Sea during glacial abrupt climate changes*** *[J]. PNAS, 2022.*

https://doi.org/10.1073/pnas.2203468119

摘要: 北大西洋和北欧海的海冰减少被认为是导致格陵兰冰芯在末次冰期记录的反复突变大气变暖的原因，被称为 Dansgaard-Oeschger (D-O)事件。然而，由于缺乏来自北大西洋西北部地区的合适高分辨率海冰代理记录，对于在 D-O 事件期间海冰变化如何与气候突变相结合的理解仍然不完整。在此，我们展示了来自 NEEM 冰芯(格陵兰岛西北部)近十年尺度的溴富集(Br_{enr})记录和沉积物芯生物标志物记录，以重建巴芬湾和拉布拉多海在 34-42 ka 之间一系列 D-O 事件中的季节性海冰变化。我们的研究结果表明，在寒冷的亚冰期中稳定、持续多年的海冰(MYSI)条件与在温暖的间冰期中不稳定的、季节性的海冰条件之间反复发生转变。随着格陵兰岛上空的大气变暖，海冰条件从亚冰期向间冰期发生迅速和同步的转变，而高频海冰波动的振幅则在间冰期升高。我们的研究结果表明，广泛的 MYSI 被季节性海冰迅速取代，放大了 D-O 事件过程中的气候突然变暖，并强调了与晚期间冰期季节性海冰扩张在推动北大西洋海洋-气候系统回到稳定状态中相关的反馈的作用。

ABSTRACT: Sea ice decline in the North Atlantic and Nordic Seas has been proposed to contribute to the repeated abrupt atmospheric warmings recorded in Greenland ice cores during the last glacial period, known as Dansgaard-Oeschger (D-O) events. However, the understanding of how sea ice changes were coupled with abrupt climate changes during D-O events has remained incomplete due to a lack of suitable high-resolution sea ice proxy records from northwestern North Atlantic regions. Here, we present a subdecadal-scale bromine enrichment (Br_{enr}) record from the NEEM ice core (Northwest Greenland) and sediment core biomarker records to reconstruct the variability of seasonal sea ice in the Baffin Bay and Labrador Sea over a suite of D-O events between 34 and 42 ka. Our results reveal repeated shifts between stable, multiyear sea ice (MYSI) conditions during

cold stadials and unstable, seasonal sea ice conditions during warmer interstadials. The shift from stadial to interstadial sea ice conditions occurred rapidly and synchronously with the atmospheric warming over Greenland, while the amplitude of high-frequency sea ice fluctuations increased through interstadials. Our findings suggest that the rapid replacement of widespread MYSI with seasonal sea ice amplified the abrupt climate warming over the course of D-O events and highlight the role of feedbacks associated with late-interstadial seasonal sea ice expansion in driving the North Atlantic ocean–climate system back to stadial conditions.

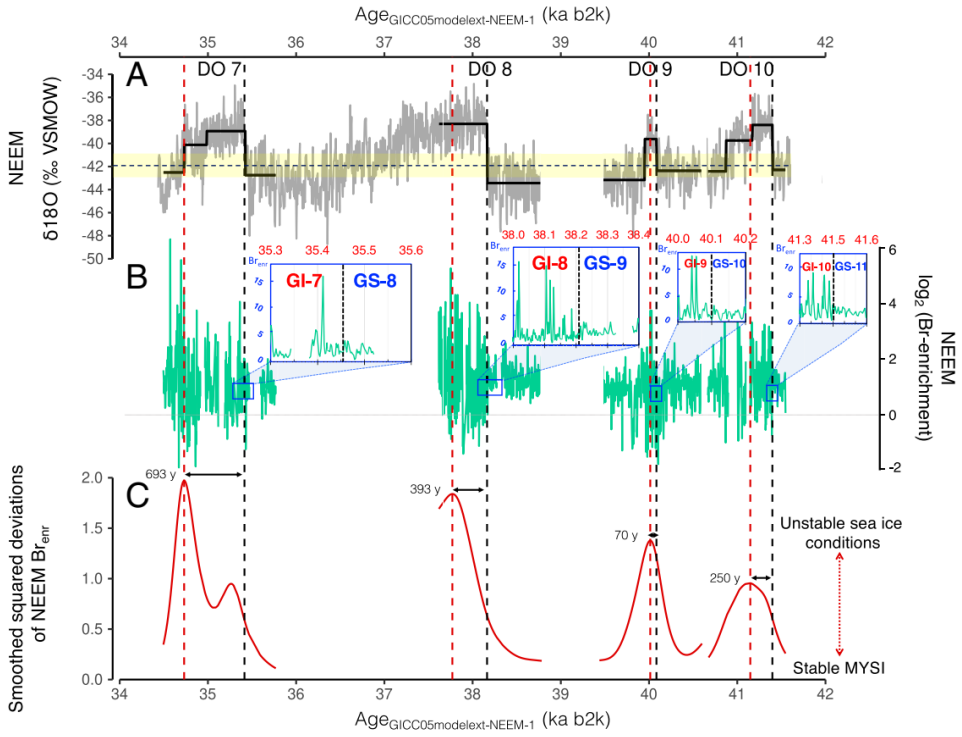

Figure 1. NEEM stable oxygen isotopes and bromine enrichment variability across D-O 7-10. (A) Black segments indicate the estimated structural changes in the $\delta^{18}O$ series; (B) NEEM Br_{enr} data plotted on a log2 scale with blown-up views centered on each stadial/interstadial transition plotted on a normal scale; (C) smoothed squared deviations from the mean of Br_{enr} series. The black vertical dashed lines indicate the onset of each D-O event using NEEM $\delta^{18}O$ data (SI Appendix, Materials and Methods for more details) while the red vertical dashed lines indicate the maxima of the smoothed squared deviations from the mean of Br_{enr}. The chronology is the GICC05modelext-NEEM-1 timescale.

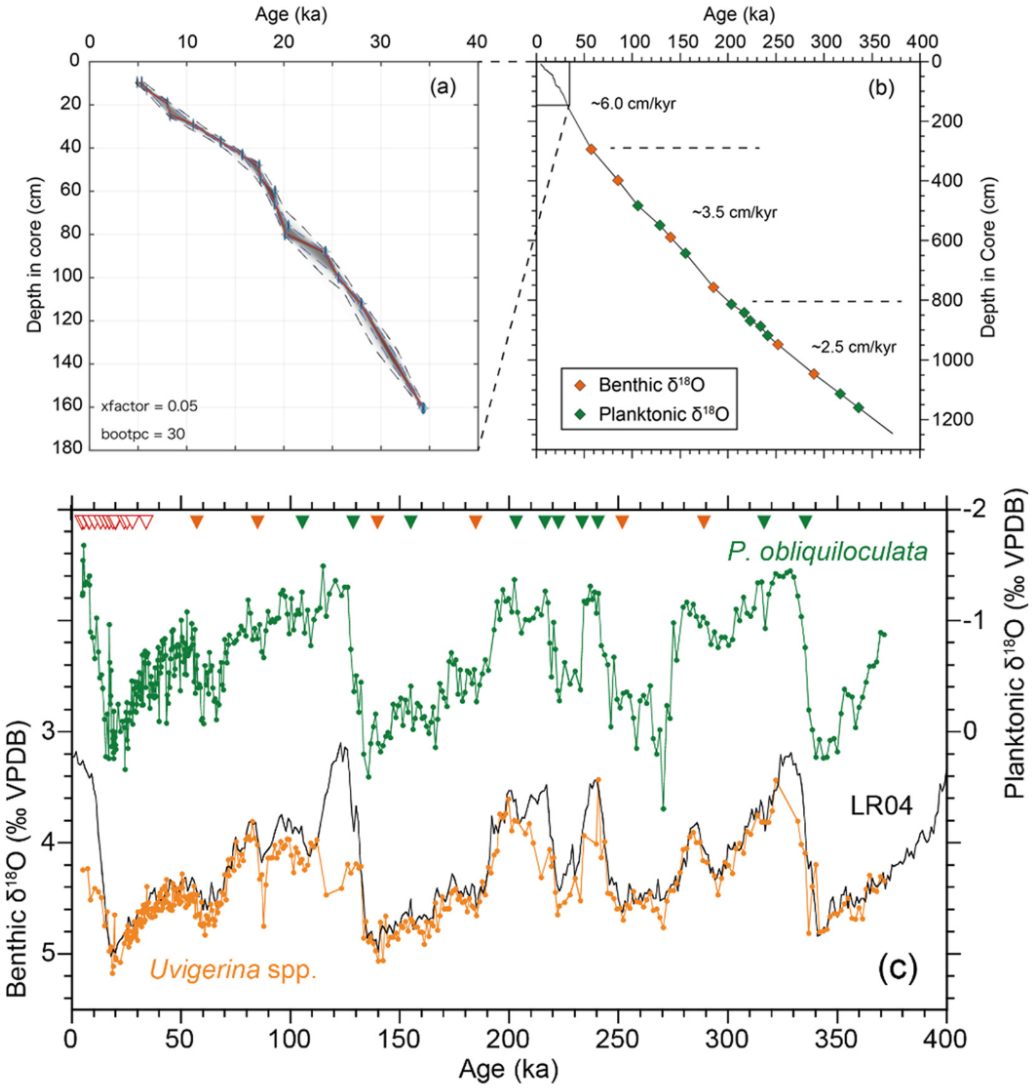

Figure 2. Sea ice reconstruction of Baffin Bay during D-O cycles 7–10. Looking at NEEM Br_{enr} profile (red curve) between, three distinct stages (A, B, C) can be identified for each D-O cycle: (A) During GS, a widespread perennial or MYSI cover spreads over Arctic Ocean and in the oceanic regions surrounding Greenland including the Baffin Bay and the Labrador Sea. (B) Synchronously or within a decade from the GI onset, the perennial sea ice edge in the Baffin Bay gradually retreats and it is partially substituted by seasonal sea ice conditions. (C) During the mid-to-late phase of the GI (~0.1–0.6 ka after the onset), highest Br_{enr} values suggest both a significant retreat of the perennial sea ice edge and/or, more likely, a major FYSI expansion southward into the western North Atlantic. In the latter scenario, the increased ice-albedo feedbacks and the enhanced sea ice export in the Labrador Sea (generating a weakening of the AMOC) culminated at or near the onset of the new stadial phase (A).

11. 南半球西部边界洋流中海洋变暖的驱动因素

翻译人：聂美娟 12232216@mail.sustech.edu.cn

Li J, Roughan M, Kerry C. ***Drivers of ocean warming in the western boundary currents of the Southern Hemisphere*** *[J]. Nature Climate Change, 2022.*

https://doi.org/10.1038/s41558-022-01473-8

摘要：南半球的西部边界流(WBCs)向两极输送热量，同时也是海洋快速变暖的地区。然而，对于南半球 WBC 扩展增强变暖的机制仍存在争议。在此我们研究得出，通过正压和斜压不稳定性的变化，WBC 扩展中增强的涡旋产生导致了当涡旋传播时海洋变暖的增强。这是由于西太平洋环流的向极移动，与中纬度东风的变化有关。因此，西暖流向两极渗透，但没有加强，现在正在向其延伸处输送更多的热量。我们的研究清楚地阐明了推动南半球 WBC 扩展区涡流和变暖增加的动力过程，对理解和预测气候变化下 WBC 扩展区的海洋变暖、海洋热浪以及对海洋生态系统的影响具有一定的意义。

ABSTRACT: Western boundary currents (WBCs) of the Southern Hemisphere transport heat poleward and are regions of rapid ocean warming. However, the mechanisms responsible for the enhanced warming over the Southern Hemisphere WBC extensions are still debated. Here we show that enhanced eddy generation in the WBC extensions through changes in barotropic and baroclinic instabilities results in enhanced ocean warming as the eddies propagate. This results from a poleward shift of the WBCs, associated with changes in the mid-latitude easterly winds. Consequently, the WBCs have penetrated poleward but not strengthened and are now transporting more heat into their extensions. Our study clearly elucidates the dynamic processes driving increased eddying and warming in the Southern Hemisphere WBC extensions and has implications for understanding and predicting ocean warming, marine heatwaves and the impact on the marine ecosystem in the WBC extensions under climate change.

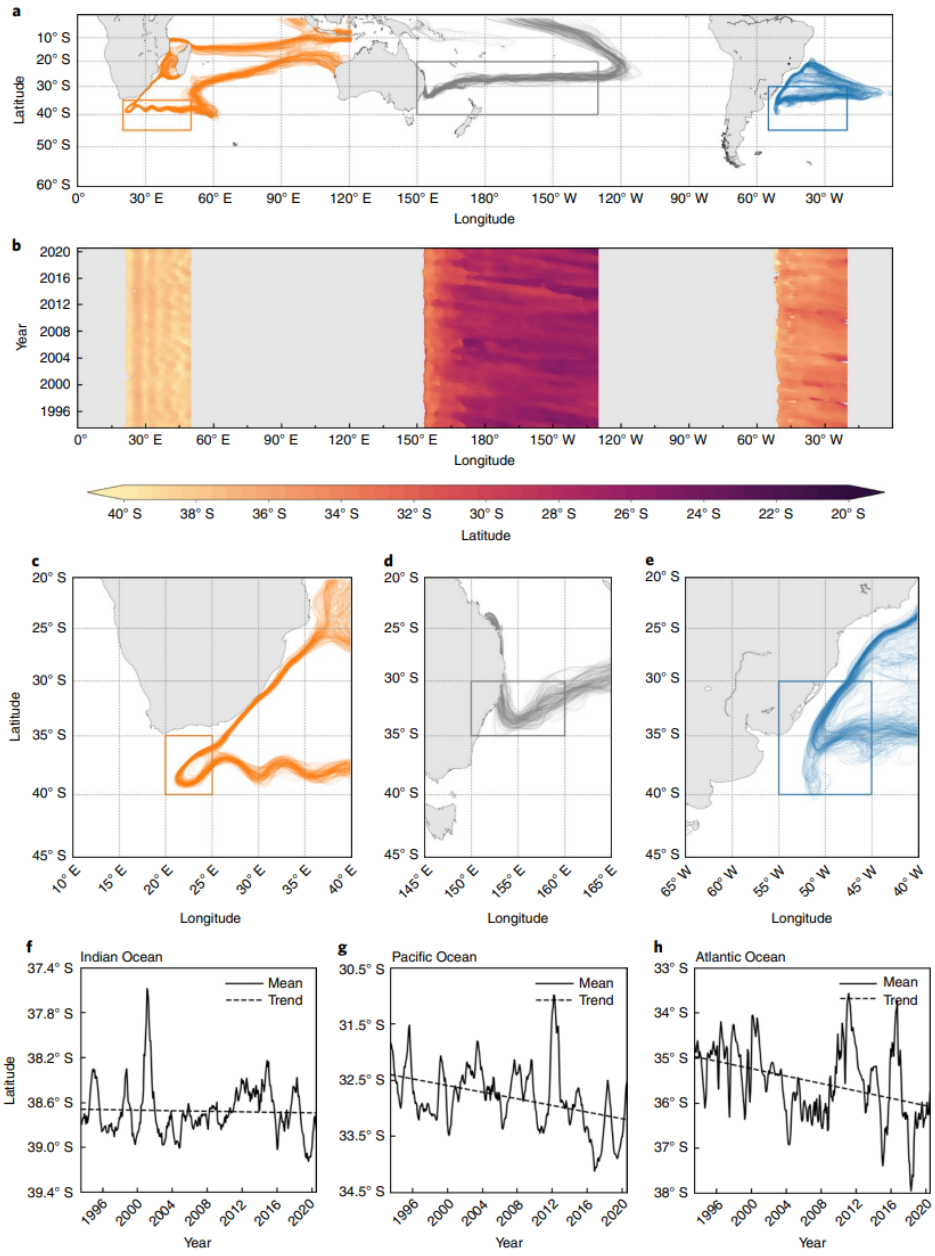

Figure 1. lustration and trends of subtropical ocean gyres in the SH. a, Monthly mean SSH contours represent the boundaries of subtropical gyres from AVISO (1993–2020). The orange lines in the Indian Ocean and the grey lines in the Pacific Ocean indicate the 0.9 m contours. The blue lines in the Atlantic Ocean indicate the 0.6 m contours. The orange, grey and blue boxes indicate the southern boundaries of subtropical gyres in each ocean basin. b, Monthly latitudinal variations of the southern boundaries of subtropical gyres. c, Monthly mean SSH contours represent the AC. The orange box indicates the AC separation region. d,e, Same as c but for the EAC (d) and BC (e) separation regions. f, Time series of

zonal mean latitudes over the AC separation region. The dashed line indicates the linear trend. g,h, Same as f but for the EAC (g) and BC (h) separation regions.

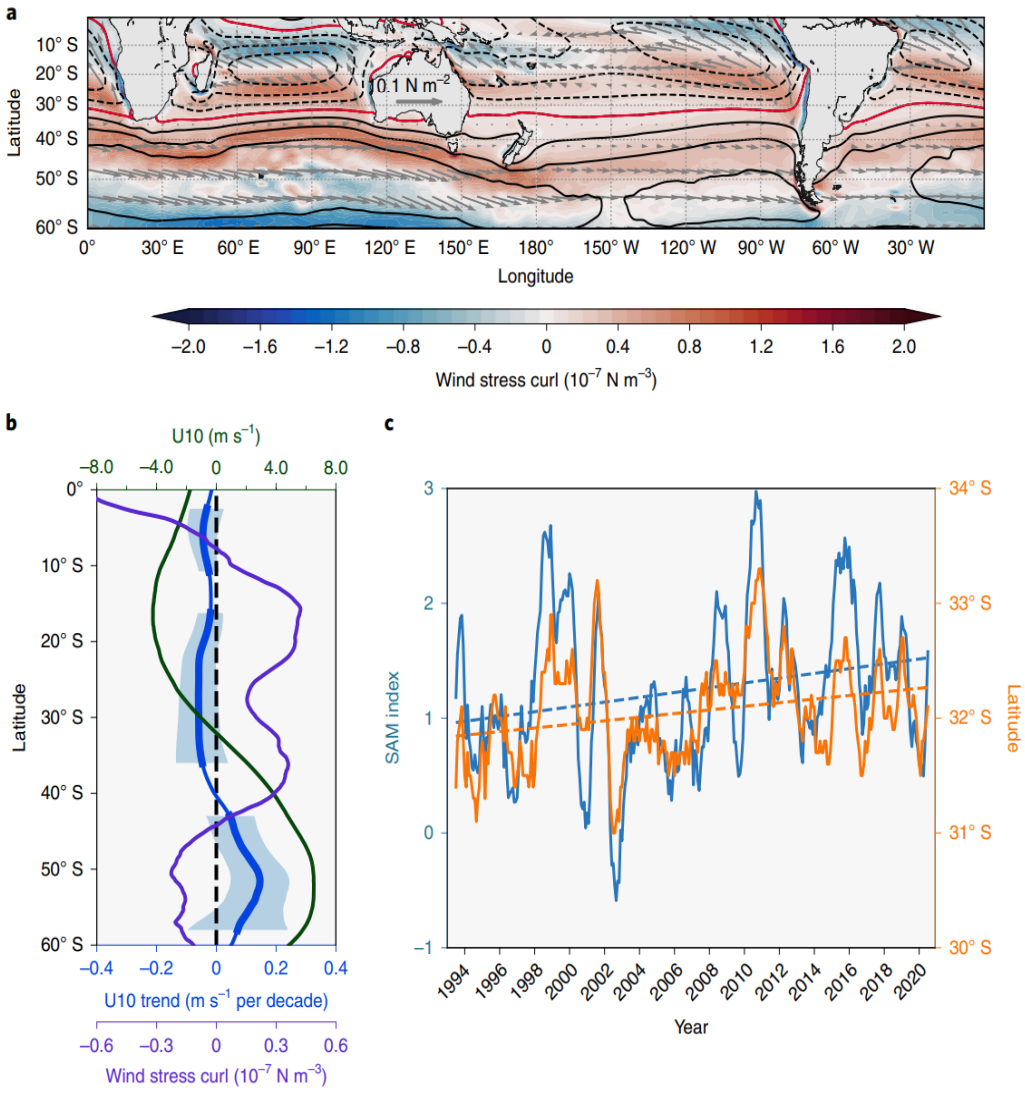

Figure 2. Large-scale wind pattern and trends associated with SAM. a, Large-scale climatological mean winds from ERA5. The shading shows wind stress curl. The grey vectors indicate the wind stress, with solid (dashed) black contours representing the westerly (easterly) winds and the solid red line denotes the zero wind stress. b, Zonal mean ocean surface winds at 10 m (U10) over the SH. The purple line, green line and blue line indicate the zonal mean climatological wind stress curl, U10 and the trends of zonal mean U10, respectively. Thick blue line and blue shading indicate the trends of zonal mean U10

that are statistically significant above the 95% confidence level and the corresponding standard errors. c, Time series of zonal mean latitudes of the zero wind stress (solid orange line) and SAM index (solid blue line). The dashed orange line and blue line indicate the linear trends of zonal mean latitudes of zero wind stress and SAM index, respectively.